Report No: TRC-EM-CAB-93003

ANTENNA PATTERN CONTROL USING IMPEDANCE SURFACES

Semiannual Progress Report
(September 16, 1992 - March 15, 1993)

by

Constantine A. Balanis and Kefeng Liu

Prepared by

Telecommunications Research Center
College of Engineering and Applied Science
Arizona State University
Tempe, AZ 85287-7206

Sponsored by

Joint Research Program Office CECOM/NASA
Langley Research Center
Hampton, VA 23681-0001

Abstract

A hybrid numerical technique is developed for electrically large pyramidal horn antennas radiating in free space. A stepped-waveguide method is used to analyze the interior surfaces of the horn transition. The Electric Field Integral Equation (EFIE) is employed on the outer surfaces of the pyramidal horn including the radiating aperture. Meanwhile, the Magnetic Field Integral Equation (MFIE) is used on the aperture to relate the aperture fields and those in the horn transition. The resultant hybrid field integral equation (HFIE) is solved numerically by the method of moments. This formulation is both accurate and numerically stable so that high-gain microwave pyramidal horns can be analyzed rigorously. Far-field radiation patterns, both computed and measured, are presented for three electrically-large X-band horn antennas. The comparisons demonstrate that this method is accurate enough to predict the fine pattern structure at wide angles and in the back region. Computed far-field patterns and aperture field distributions of two smaller X-band horns are also presented along with a discussion on the validity of the approximate aperture field distributions routinely used in the analysis and design of pyramidal horns.

I. Introduction

The horn antenna is the simplest and probably the most widely used microwave radiator. It is used as the feed for large reflector and lens antennas in communication systems throughout the world. It is also a high gain element in phased arrays. Since horn antennas are highly accurate radiating devices, they are often used as standard-gain devices for the calibration of other antennas. The application of electromagnetic horns has been explored for nearly a century. Extensive investigations of horn antennas have been of increasing interest during the past three decades. Some of the early research papers on horn antennas are well documented in Love's collection[1]. In applications, the pyramidal geometry has been a preferred configuration. Besides being a high-gain and high-efficiency microwave antenna, the pyramidal horn exhibits some additional advantages. Its rectangular geometry leads to ease of construction and to a low-cost device. The aperture size of the horn can be adjusted to achieve specific beam characteristics with negligible changes in others. It is also easy to excite the pyramidal horn with conventional microwave circuit devices. These advantages distinguish the pyramidal horn as a preferred microwave radiator.

The analysis and design of the pyramidal horns are traditionally carried out by using approximate aperture field distributions, and assuming that contributions from induced currents on other parts of the horn surface are negligible. A quadratic phase term is usually assumed to account for the flaring of the horn transition [2, 3, 4]. This approximate method predicts fairly well the main-beam of the far-field radiation pattern and the gain of the antenna. Since reflections, mode couplings, and diffracted fields from the exterior surfaces are not included, it does not predict very well sidelobes and the pattern structure in the back region.

In the 1960's, the Geometric Theory of Diffraction (GTD), a high- frequency method, was introduced to include edge diffracted fields. The two-dimensional GTD model presented in [5, 6] yielded an improvement in the far-field E-plane pattern over the approximate aperture field method. A two-dimensional model for the E-plane pattern based on an integral equation and the Moment Method was examined by Botha *et al.* in [7]. Although, the two-dimensional models are in better agreement with measured far- field E-plane patterns, they

cannot duplicate the H-plane pattern in the back regions since couplings of the diffracted fields from both the E- and H-plane edges are not included in the two-dimensional models. Finally, neither the approximate aperture field method nor the GTD are well suited for calculating the aperture field distribution, VSWR, and cross-polarized patterns.

A rigorous analysis of pyramidal horn antennas was deemed a formidable task in the early development of horn antennas. Recent advances of the computational capabilities and the popularity of the pyramidal horn antennas have encouraged the development of more accurate models with improved numerical efficiencies. The integral equation formulation with a Moment Method (MM)[8] solution has become a powerful tool in modeling complex electromagnetic field problems. MM has been used to analyze an aperture in a ground plane[9, 10] and a grounded aperture in the presence of a thin conducting plate[11]. It has been applied to pyramidal horn antennas, both with and without corrugations, mounted in a ground plane[12, 13]. The presence of a ground plane simplifies the analysis; however for most applications, the horn antenna is a stand-alone radiating element. Without the ground plane, electric current is induced on the outer surfaces which has a significant impact on the pattern at wide angles and in the rear hemisphere.

Complete three-dimensional models have been developed for electrically small pyramidal horn antennas has been analyzed using MM[14], and small H-plane sectoral horns and X-band standard-gain horns by the finite-difference time- domain method (FDTD)[15, 16]. For high gain pyramidal horn antennas, it is a difficult task to model antennas very accurately with a simple extension of existing numerical electromagnetic methods, such as those described in [14, 15, 17, 16]. The main problem in modeling the transition from a relatively small feeding aperture to a much larger radiating aperture is the use of an efficient number of elements. The electric current densities on the interior surfaces of the horn transition becomes too complex to be modeled effectively using these methods.

A full-wave stepped-waveguide model and HFIE method to analyze both the interior flaring and the exterior current contributions was previously developed by Kühn et al [18] for conical horns, whose formulation is simplified due to their axial symmetry. This paper follows a similar procedure as [18] to solve horns with square and rectangular geometries.

This full-wave formulation provides flexibility and includes all of the important details of a practical pyramidal horn antenna. It represents the first full-wave method to include the current densities on all conducting surfaces of a pyramidal horn which are necessary to predict the fine pattern structure in regions of low-level radiation, such as those in the outermost minor lobes.

II. Theory

Figure 1 illustrates the geometry of a typical pyramidal horn antenna. The field problem can be separated into two parts. The first is the transition from the feeding waveguide to the radiating aperture. A complete full-wave approach to this part of the problem is to represent the transition as a series of stepped-waveguide sections as shown in Figure 2. Mode matching is performed by rigorously enforcing the boundary conditions at each step. The result is a scattering matrix for each step which can be combined to obtain a scattering matrix for the entire transition region.

The second part of the problem is an aperture radiating in the presence of the exterior conducting surfaces, as shown in Figure 3. Interactions between the aperture fields and the exterior surfaces of the horn will impact the radiation pattern as well as the field in the transition region. The interaction is accurately analyzed by using the EFIE on the exterior surfaces of the horn. The equivalence principle is introduced to formulate the magnetic field integral equation on the radiating aperture which combines the interior field transition problem with the exterior radiation.

Because of the decomposition of the problem into interior and exterior part, there is sufficient flexibility in choosing the methods and numerical models for the solution of each parts. Therefore, an accurate analysis of the transition and the exterior surfaces can be implemented robustly and efficiently.

A. Interior Horn Transitions

An accurate analysis of waveguide transitions has been an interesting research topic in the microwave circuit design [19, 20, 21, 22]. The available numerical approaches can be

divided into two classes: a numerical solution of the system of ordinary differential equations [20, 23], and the stepped waveguide model with a full-wave mode-matching technique on stepped junctions [19, 13, 23, 18]. The numerical solution of the differential equations must be performed with a finite advancing step size, and due to the numerical problem caused by evanescent modes, the taper has to be divided into several sections. The hybrid matrix of each section needs to be computed separately, then translated and combined into a scattering matrix. On the other hand, the stepped-waveguide technique uses a finite number of subdivisions of waveguide steps to approach the continuous horn taper. Within each waveguide step, the waveguide section is uniform. The scattering matrices of each waveguide step are related to each other by the electromagnetic boundary conditions on the discontinuous junctions connecting them. The combination of the scattering matrices of all the steps gives the total scattering matrix of the horn transition. As examined by [21] and [23], the numerical technique that solves the first-order differential equation yields results with the same accuracy as given by the stepped-waveguide technique, when the size of the steps is sufficiently small. The validity of the stepped-waveguide approximation to simulate the continuous horn transition has been justified in [12, 13, 23, 18, 19]. The computational effort for the two approaches is about the same.

In this paper, the stepped waveguide technique is employed for its advantage in the numerical stability. Figure 2 represents a typical stepped waveguide model of the horn transition. The continuous transition is approximated by a number of cascaded stepped-waveguides, and for a pyramidal horn transition, each step is a section of rectangular waveguide. Electromagnetic field distributions in each of the rectangular sections can be expressed as the superposition of all possible TM_z and TE_z modes. Moreover, the TM_z and TE_z modes in each region can be generated by the z components of two vector potentials[24]

$$F_z = \epsilon \sum_{\substack{m=1,M \\ n=0,N}} (A_{mn}e^{-j\beta_z z} + B_{mn}e^{j\beta_z z})e_{mn}(x,y) \tag{1}$$

$$A_z = \sqrt{\mu\epsilon} \sum_{\substack{m=1,M \\ n=2,N}} (C_{mn}e^{-j\beta_z z} - D_{mn}e^{j\beta_z z})h_{mn}(x,y) \tag{2}$$

$$e_{mn}(x,y) = \frac{2\cos(\beta_x x)\cos(\beta_y y)}{\beta_c\sqrt{ab(1+\delta_{no})}} \quad ; \quad h_{mn}(x,y) = \frac{2\sin(\beta_x x)\sin(\beta_y y)}{\beta_c\sqrt{ab}}$$

$$\beta_x = \frac{m\pi}{a};\ \beta_y = \frac{n\pi}{b};\ \beta_c = \sqrt{\beta_x^2+\beta_y^2} \quad ; \quad \beta_c^2+\beta_z^2 = \omega^2\mu\epsilon;\ \delta_{no} = \begin{cases} 1 & \text{if n=0} \\ 0 & \text{otherwise} \end{cases}$$

The electric and magnetic fields are obtained from the vector potentials as described in [24]. At the stepped waveguide junction, the boundary conditions relating the two slightly differently sized waveguides are

$$E_{x,y}^{(1)}(x,y)|_{\text{on } S} = E_{x,y}^{(2)}(x,y)|_{\text{on } S} \tag{3}$$

$$E_{x,y}^{(2)}(x,y)|_{\text{on } \Delta S} = 0 \qquad \Delta S \nearrow \boxed{S} \tag{4}$$

$$H_{x,y}^{(1)}(x,y)|_{\text{on } S} = H_{x,y}^{(2)}(x,y)|_{\text{on } S} \tag{5}$$

where S is the area of the smaller waveguide section, and ΔS the "ring" area of the larger waveguide section extracting S as illustrated in Figure 4. Testing the boundary conditions in (3) -(5) by the corresponding expansion functions (this process is equivalent to a full-domain Galerkin's Method), the boundary conditions uniquely define the relation between the full-wave expansion coefficients on both sides of the junction. The details of the matching at the discontinuities and the combination of the scattering matrices are available in[21, 19, 18, 12, 23, 13]. If all incident full-wave modes are represented by a vector **a** and the reflected full-wave modes by a vector **b**, the two are related by the total scattering matrix for the horn transition as

$$\begin{pmatrix} \mathbf{b}^{(F)} \\ \mathbf{a}^{(A)} \end{pmatrix} = \begin{pmatrix} \mathbf{S}_{11}^{(T)} & \mathbf{S}_{12}^{(T)} \\ \mathbf{S}_{21}^{(T)} & \mathbf{S}_{22}^{(T)} \end{pmatrix} \begin{pmatrix} \mathbf{a}^{(F)} \\ \mathbf{b}^{(A)} \end{pmatrix} \tag{6}$$

where superscripts '(F)' and '(A)' denote, respectively, the full- wave coefficients at the feed junction and radiating aperture, and the superscript '(T)' denotes the total contribution of the horn transition. Although pyramidal horns are generally excited by the dominant TE_{10} mode from the feeding waveguide, higher order TE_{mn} and TM_{mn} modes are generated in the transition. For horn geometries with symmetrical flarings in both dimensions, only those modes which have $m = 1,3,5,7,...,M$ and $n = 0,2,4,6,...,N$ ($n = 0$ for TE modes

only) are generated in the transition. The coupling between TE_{mn} and TM_{mn} modes is automatically included in the full-wave analysis of the stepped junctions.

There are two factors which affect the accuracy of the stepped- waveguide approximation: the size of the steps and the number of terms in the series (M and N in (1)-(2)). Past experience demonstrates that a convergence is achieved by limiting the maximum size of the steps to $\lambda/32$. The choice of M and N should be based on the flare angle and length of the steps. It is important to keep a sufficient number of terms in the series because higher order modes at the aperture contribute significantly to the radiation pattern in the back regions. Therefore, significant more terms are needed for this analysis than that performed in [12, 13]. An empirically derived formula for determining M and N is the nearest higher integer of

$$(M, N) = \frac{3(A, B)}{\lambda} + 1.5 \tag{7}$$

where A and B are the dimensions of the horn aperture. When analyzing a high-gain horn antenna, the required number of modes determined by (7) is large, and if used throughout the matching process, the computation could become very inefficient. To reduce the computation time, a variable number of modes can be used along the transition. At each step, the number of modes are determined using the same criterion given for the aperture in (7) except A and B are replaced by the step dimensions. Therefore, only a few modes are required near the feed and approach (7) as the computation proceeds toward the horn aperture. This process preserves accuracy, and for the geometries considered here, reduces the computation time to about one eighth that of a constant number of modes.

B. Integral Equations and Moment Method

The radiation from the aperture and the outer surface of the pyramidal horn are analyzed using a Moment Method solution to integral equations [8, 24]. Since the outer surfaces of a high-gain pyramidal horn antenna are usually $120\lambda^2$ to $200\lambda^2$, a straight-forward Moment Method solution is a very computationally involved process. Therefore, a variety of theoretical and numerical techniques are introduced to enhance the efficiency and accuracy

of the solution.

1. The Hybrid Field Integral Equation

Figure 3 presents the general problem of a radiating aperture in a conducting body. In Figure 3, the fields internal to the aperture are represented by the full-wave vectors **a** (the incident mode) and **b** (the reflected modes). To relate the internal and external fields on the aperture, *Love's field equivalence principle* [24] is introduced. The radiating aperture is replaced by a sheet of perfect electric conductor with a magnetic current density

$$\mathbf{M}(\mathbf{a}^{(A)} + \mathbf{b}^{(A)}) = -\mathbf{n} \times \mathbf{E}^{int}(\mathbf{a}^{(A)}, \mathbf{b}^{(A)}) \tag{8}$$

where $\mathbf{n}$ is the unit vector normal to the aperture, and $\mathbf{E}^{int}(\mathbf{a}^{(A)}, \mathbf{b}^{(A)})$ is the electric field internal to the aperture. Equation (8) insures the continuity of tangential electric fields across the aperture. The magnetic current density $\mathbf{M}$ is radiating in the presence of the closed conducting surfaces of the horn. An electric surface current is then induced to maintain zero tangential electric field on the external surfaces of the horn. Therefore, the continuity of the tangential magnetic field across the aperture and the boundary conditions on the external surfaces require that

$$\mathbf{H}^{ext}_{tan}(\mathbf{M}) + \mathbf{H}^{ext}_{tan}(\mathbf{J}) = \mathbf{H}^{int}_{tan}(\mathbf{a}^{(A)}, \mathbf{b}^{(A)}) \quad \text{on the aperture} \tag{9}$$

$$\mathbf{E}^{ext}_{tan}(\mathbf{J}) + \mathbf{E}^{ext}_{tan}(\mathbf{M}) = 0 \quad \text{on the external surfaces and the aperture} \tag{10}$$

where field components with 'ext' denote the fields on the free space side of the aperture. The boundary conditions of (8)-(10) derived from *Love's field equivalence principle* satisfy the uniqueness theorem and define an equivalent to the actual electromagnetic problem.

2. Moment Method Solutions

In the Moment Method solution of the hybrid field integral equations of (8) and (10), sub-sectional quadrilateral roof-top patch modes are chosen as both the expansion and testing functions for the electric current density distribution on the exterior surfaces of the horn.

To exploit the Toeplitz property of the impedance matrix elements, magnetic current density on the aperture is also expanded and tested with the same roof-top patch modes as those of electric current modes on the aperture. Thus, impedance and admittance matrix elements for the integral equation solution on the aperture are related and do not have to be computed twice. A more detailed explanation of such a process can be found in [17]. Since the aperture magnetic current density is related to the full-wave modes $\mathbf{a}^{(A)}$ and $\mathbf{b}^{(A)}$, a conversion matrix is introduced to transform the roof-top patch modes into eigen modes of the aperture field in (8)

$$\mathbf{J} = \sum_{i=1}^{N_J} J_i \mathbf{P}_i^J \qquad \mathbf{M} = \sum_{i=1}^{N_M} M_i \mathbf{m}_i = \sum_i M_i \sum_{j=1}^{N_A} V_{ij} \mathbf{P}_j^M \tag{11}$$

where $\mathbf{P}_i^J$ and $\mathbf{P}_j^M$ are the subsectional roof- top patch modes for the i-th electric and j-th magnetic current density modes, respectively. N_M represents the total number of full- wave expansion modes of both TE and TM in the aperture, N_A represents the number of roof-top patch modes for the aperture magnetic current density and N_J represents the total number of roof-top patch modes for the electric current density on the entire outer surface of the horn including the aperture. $[V_{ij}]$ is the conversion matrix from the distribution functions of the aperture modes $\mathbf{m}_i$ expressed by $e_{mn}(x,y)$ and $h_{mn}(x,y)$ in (1) and (2) to the roof-top patch modes. Testing (10) with $\mathbf{P}_i^J$ leads to

$$- < \mathbf{P}_i^J, \mathbf{E}_{tan}^{ext}(\mathbf{J}) > = < \mathbf{P}_i^J, \mathbf{E}_{tan}^{ext}(\mathbf{M}) > \tag{12}$$

Substituting the expansion representation of $\mathbf{J}$ and $\mathbf{M}$ into (12), yields a matrix with elements given by

$$Z_{ij} = -\frac{1}{\eta} < \mathbf{P}_i^J, \mathbf{E}_{tan}^{ext}(\mathbf{P}_j^J) > \; = \; -\frac{1}{\eta} \int_{S_i} \int_{S_j} \mathbf{P}_i^J \cdot \mathbf{E}_{tan}^{ext}(\mathbf{P}_j^J) ds_i ds_j \tag{13}$$

$$Q_{kl} = < \mathbf{P}_k^J, \mathbf{E}_{tan}^{ext}(\mathbf{P}_l^M) > \; = \; \int_{S_k} \int_{S_l} \mathbf{P}_k^J \cdot \mathbf{E}_{tan}^{ext}(\mathbf{P}_l^M) ds_k ds_l \tag{14}$$

A normalization factor of $1/\eta$ is introduced in computing the matrix elements of Z_{ij} in (13) to reduce rounding errors in combining big matrices, which is very helpful in maintaining the numerical stability of the MFIE in (9). Efficient and accurate algorithms for evaluating the

four-fold integral of (13) and (14) are briefly described in Appendix A. Since the expansion and the testing modes are the same, the impedance matrix $\mathbf{Z}$ is a complex symmetric matrix. It can be filled and decomposed with only half of the CPU time needed for the full-matrix system[25, 26]. The solution of (12) leads to

$$\mathbf{J} = \frac{1}{\eta}\mathbf{Z}^{-1}\mathbf{U}\mathbf{M} \tag{15}$$

where

$$\mathbf{U} = \mathbf{Q}\mathbf{V}^t \tag{16}$$

and the superscript 't' signifies transpose. $\mathbf{J}$ is the vector representation of the subsectional roof-top patch modes and $\mathbf{M}$ the aperture field modes. The transformation from $\mathbf{Q}$ to $\mathbf{U}$ in (16) reduces the number of right-hand side solution from N_A to N_M (N_M is generally a small fraction of N_A). Again, testing (9) with $\mathbf{m}_i$, the MFIE can be expressed as

$$< \mathbf{m}_i, \mathbf{H}_{tan}^{ext}(\mathbf{M}) > + < \mathbf{m}_i, \mathbf{H}_{tan}^{ext}(\mathbf{J}) >=< \mathbf{m}_i, \mathbf{H}_{tan}^{int}(\mathbf{a}^{(\mathbf{A})}, \mathbf{b}^{(\mathbf{A})}) > \tag{17}$$

Using duality for the reaction of the aperture magnetic current density modes[17], reciprocity for the reactions between the aperture magnetic modes and the outer surface electric modes, and the relation of (13), equation (17) can be written as

$$\mathbf{b}^{(A)} = \mathbf{S}^{(A)_{11}}\mathbf{a}^{(A)} \;=\; [\mathbf{Y}^{(A)} + \mathbf{Y}^{int}]^{-1}[\mathbf{Y}^{int} - \mathbf{Y}^{(A)}]\mathbf{a}^{(A)} \tag{18}$$

where $\mathbf{I}$ is the identity matrix, $\mathbf{Y}^{(A)}$, and $\mathbf{Y}^{(int)}$ the aperture admittance matrices defined by

$$\mathbf{Y}^{(A)}(\mathbf{a}^{(A)} + \mathbf{b}^{(A)}) \;=\; [\mathbf{V}\mathbf{Z}^{(A)}\mathbf{V}^t + \mathbf{U}^t\mathbf{Z}^{-1}\mathbf{U}][< \mathbf{m}_i, \mathbf{M}(\mathbf{a}^{(A)} + \mathbf{b}^{(A)}) >] \tag{19}$$

$$\mathbf{Y}^{int}(\mathbf{a}^{(A)} - \mathbf{b}^{(A)}) \;=\; [< \mathbf{m}_i, \eta\mathbf{H}_{tan}^{int}(\mathbf{a}^{(A)} - \mathbf{b}^{(A)}) >] \tag{20}$$

$\mathbf{Z}^{(A)}$ is a subset of $\mathbf{Z}$ for electric current density modes on the aperture. Using (18) and (6), the incident aperture field distribution coefficients (denoted by a vector $\mathbf{a}^{(A)}$) and the reflected wave at the feed (denoted by a scalar coefficient $b_{10}^{(F)}$) are given by

$$\mathbf{a}^{(A)} = (\mathbf{I} - \mathbf{S}_{22}^{(T)}\mathbf{S}^{(A)})^{-1}\mathbf{S}_{21}^{(T)}a_{10}^{(F)} \quad (21)$$

$$b_{10}^{(F)} = [\mathbf{S}_{11}^{(T)} + \mathbf{S}_{12}^{(T)}\mathbf{S}^{(A)}(\mathbf{I} - \mathbf{S}_{22}^{(T)}\mathbf{S}^{(A)})^{-1}\mathbf{S}_{21}^{(T)}]a_{10}^{(F)} \quad (22)$$

where $a_{10}^{(F)}$ is the magnitude of the incident TE_{10} mode in the feeding waveguide. Equations (22), (21), (18), and (15) specify the antenna reflection coefficient (or return loss), the aperture magnetic current density distributions, and the electric current density distributions on the exterior surfaces. The radiated electric field can be determined from the current density expansions and the gain computed from

$$G(\theta,\phi) = 10\log_{10}\frac{|\mathbf{E}(\mathbf{J},\theta,\phi) + \mathbf{E}(\mathbf{M},\theta,\phi)|^2}{4\pi|a_{10}^{(F)}|^2\sqrt{1-(\frac{f_c}{f})^2}} \quad (23)$$

where f_c is the cut-off frequency of the feeding waveguide, and f the operating frequency.

III. Results and Discussions

Five X-band high-gain pyramidal horns were chosen to be analyzed. For the quadrilateral roof-top expansion of the exterior surfaces of the horn at 10 GHz, Table 1 gives the dimensions and typical computed data for a maximum segment length of 0.15λ for the 10- and 15-dB standard gain horn, and 0.2λ for the other three horns. The CPU times are typical for an IBM R6000-350 workstation. Table 2 lists gains and VSWR's obtained by the approximate aperture method and the Moment Method (MM). As expected, differences are more obvious for the 10-dB gain horn since the approximate method in [4] does not work very well for such a small horn. Table 3 lists comparison of approximate, measured, and predicted gains and VSWR's for the 20-dB X-band standard gain horn antennas at three different frequencies. Note that the gains listed in the tables have almost a constant 0.2 dB differences between the moment method solution and the measured data. Nearly the same amount of difference is observed between computed and measured gains for the other two large X-band square aperture horns. It should be mentioned that the same 20-dB standard-gain horn is used as the calibration antenna. Therefore, if there is any inaccuracy in the calibration data, all measured data sets are affected. The agreement between the

Table 1: Typical data of pyramidal horn antennas analyzed

	Pyramidal horn dimensions A	B	L	EFIE Matrix size(# of rows)	CPU (in hrs)
10-dB Standard-gain horn	1.58″	1.15″	2.01″	820	0.38
15-dB Standard-gain horn	2.66″	1.95″	5.46″	1600	0.61
20-dB Standard-gain horn	4.87″	3.62″	10.06″	4300	1.8
5-inch square horn	5.04″	5.06″	10.5″	5700	2.6
7-inch square horn	7.0″	7.0″	12.1″	9600	11.3

Table 2: Comparison of VSWR's and gains of 10- and 15-dB standard gain horns

		8.2 GHz VSWR	Gain	10.3 GHz VSWR	Gain	12.4 GHz VSWR	Gain
10-dB Horn	Approximate	N/A	8.98 dB	N/A	11.13 dB	N/A	12.81 dB
	MM	1.18	9.75 dB	1.17	11.63 dB	1.20	13.48 dB
15-dB Horn	Approximate	N/A	13.83 dB	N/A	15.83 dB	N/A	17.42 dB
	MM	1.11	14.23 dB	1.14	15.94 dB	1.10	17.58 dB

Table 3: Comparison of VSWR's and gains of the 20-dB standard gain horn

	9 GHz VSWR	Gain	10 GHz VSWR	Gain	11 GHz VSWR	Gain
Approximate	N/A	19.77dB	N/A	20.59dB	N/A	21.31dB
MM	1.082	19.98dB	1.057	20.63dB	1.031	21.46dB
Measured	1.10	19.72dB	1.06	20.46dB	1.04	21.24dB

computed and measured VSWR's is excellent. Figures 5 to 6 present comparisons of E- and H-plane patterns obtained from the moment method and the approximate method for the two smaller X-band horns. The approximate patterns are computed using the method outlined in Chapter 12 in [4], except that the free-space wave impedance in (12.1d) is replaced by the guide wave impedance at the aperture. As expected, the agreement of the patterns in Figure 5 is not as good as in Figure 6. Figure 7 shows the comparison of the moment method, approximate, and measured E- and H-plane patterns for the 20-dB standard gain horn. Since the horn is much larger than the previous two horns, the approximate method compares well with measurements in the first few lobes of the patterns. However, patterns predicted using the moment method compare much better with the measured patterns. The

improvement over the approximate method is more evident in the back regions.

In 1965, Russo *et. al.* [5] presented investigations into the effect of different wall thicknesses on E-plane patterns of pyramidal horn using GTD. Figure 8 presents our comparisons of the E- and H-plane patterns of the 5-inch square X-band horn at 10.0 GHz with and without modeling the aperture wall thickness. Results in the figures agree with Russo's conclusion for the E-plane radiation patterns. However, for the H-plane patterns, the predicted patterns of the thin wall model do not agree in the back region with the measured patterns as well as those of the thick wall model. The thick wall model accurately predicts the fine ripple structure in the back region while the thin wall model does not. It is our observation that the aperture wall thickness plays a significant role in affecting the fine ripple structures of the H-plane patterns. The addition of the outer surface of the feeding structure in the EFIE has only a negligible effect on the patterns of the horn antennas and does not change any ripple structure in the backlobes.

Another advantage of the moment method solution is the ability to examine the aperture field distribution. Figures 9 to 11 represent computed aperture field (E_y and H_x components) distributions of the three X-band pyramidal horns at 10 GHz. Contrary to the approximation that the aperture fields are basically TE_{10} with parabolic phase fronts, the distributions computed by the moment method demonstrate a much more complicated shape. The deviations from the approximate aperture distributions are more evident for H_x. Figures 9 to 11 also illustrate that as the electrical size of the aperture become larger, the amplitude distributions become more complicated, but the phase distributions approach a parabolic phase front as assumed by the approximate method.

As presented in the comparisons between computed and measured results, the full-wave and HFIE method has demonstrated an excellent accuracy in simulating both small and large pyramidal horn antennas. One of the requirements for this method in solving large pyramidal horns is the computer memory. In some workstations such as the IBM RS6000/350, the fast data transferring capability between the memory and the hard-disk enables the out-of-core memory matrix solver for a symmetric complex system to run nearly as fast as the in-core solver. If the symmetric property of the electric current distribution

on the exterior surfaces is utilized, the memory can be reduced to 1/8 while the CPU time can be decreased to about 1/4 of the values listed in Table 1.

IV. Conclusions

A full-wave hybrid field integral equation method has been developed to analyze pyramidal horns. The model includes the current induced on the exterior surfaces and has been verified by a comparison of computed and measured data. For accurate results, the following guidelines are suggested:

- include a sufficient number of higher order modes in the full- wave analysis. The required number of modes can be determined using the empirical formula of (7).
- limit the size of the stepped discontinuity to less than $\lambda/32$ when approximating the continuous horn transition.
- limit the largest segment size of the roof-top patch to less than 0.2λ to ensure an effective and accurate solution of the electric field integral equation on the outer surfaces of the pyramidal horn.
- include the wall thickness in the segmentation of the outer surface.

This study shows that the approximate method found in most antenna books is not very accurate in predicting gains and patterns of the pyramidal horns of small electrical size. However, as the electrical size gets larger, the approximate method becomes more accurate in predicting the gains and the first few minor lobes of the far-field radiation patterns of a pyramidal horn. The aperture field distributions of pyramidal horns are much more complicated than those assumed in the approximate formula. However, the phase distribution approaches a parabolic distribution for apertures of large electrical sizes.

Although the moment method solution is somewhat computationally intensive, a widespread application of high power workstations, such as the IBM RISC6000 platforms, is making it more effective to serve as a computer-aided analysis and design tool. Although the present development has concentrated on pyramidal horn antennas, the model can be extended to analyze wide-band dual-ridged, and quadruple-ridged horns.

V. Appendices

A. Evaluation of the Impedance Matrix Elements in Moment Method

The electric fields due to surface electric and magnetic current distribution needed in (13) and (14) can be written as

$$\mathbf{E}(\mathbf{J}) = -j\beta\eta \int_{S'} (\mathbf{J}(\mathbf{s}') + \frac{1}{\beta^2}\nabla\nabla' \cdot \mathbf{J}(\mathbf{s}'))\Phi ds' \tag{A.1}$$

$$\mathbf{E}(\mathbf{M}) = -\int_{S'} \mathbf{M}(s') \times \nabla\Phi ds' \tag{A.2}$$

where primed coordinate represents the source coordinate and $\Phi = e^{-j\beta R}/4\pi R$ is the free-space Green's function; $\mathbf{J}(s')$ and $\mathbf{M}(s')$ are surface electric and magnetic current density on S', respectively. Substituting (A.1) and (A.2) into (13) and (14), respectively, using the current continuity condition, the impedance matrix elements can be expressed in the form of

$$Z_{ij} = j\beta \int_{S_i} \int_{S'_j} [(\mathbf{P}_i^J \cdot \mathbf{P}_j^J) - \frac{1}{\beta^2}(\nabla \cdot \mathbf{P}_i^J)(\nabla' \cdot \mathbf{P}_j^J)]\Phi ds'_j ds_i \tag{A.3}$$

$$Q_{kl} = \beta \int_{S_k} \int_{S'_l} \frac{\mathbf{n} \cdot \mathbf{R}}{R^2} P_k^J(s_k) P_l^M(s'_l)(1 + j\beta R)\Phi ds'_l ds_k \tag{A.4}$$

where $\mathbf{n}$ is the unit directional vector of $(\mathbf{P}_k^J \times \mathbf{P}_l^M)$. Evaluations of (A.3) and (A.4) can be efficiently carried out by using Taylor's expansions of the kernel functions Φ and $e^{-j\beta R}$ at the center of the two patches and analytical integrations can be found for individual terms of the Taylor's expansions. Therefore, only one of the surface integrals needs to be evaluated numerically.

References

[1] A. W. Love, *Electromagnetic Horn Antennas.* IEEE Press Selected Reprint Series, IEEE Press, 1976.

[2] H. Jasik, ed., *Antenna Engineering Handbook.* McGraw-Hill, 1961.

[3] R. S. Elliott, *Antenna Theory and Design.* Prentice Hall, 1981.

[4] C. A. Balanis, *Antenna Theory: Analysis and Design.* Wiley, 1982.

[5] P. M. Russo, R. C. Rudduck, and L. J. Peters, "A method for computing E-plane patterns of horn antennas," *IEEE Trans. Antennas Propagat.*, vol. AP-13, pp. 219–224, Mar. 1965.

[6] J. S. Yu, R. C. Rudduck, and L. J. Peters, "Comprehensive analysis for E-plane of horn antennas by edge diffraction theory," *IEEE Trans. Antennas Propagat.*, vol. AP-14, pp. 138–149, Mar. 1966.

[7] L. Botha and D. A. McNamara, "Examination of antenna patterns of profiled horns using the method of moments," *IEEE Antennas Propagat. Soc. Int. Symp. Dig.*, vol. I, Vancouver, pp. 293–296, June 1985.

[8] R. F. Harrington, *Field Computation by Moment Methods.* Krieger, 1968.

[9] J. R. Mautz and R. F. Harrington, "Transmission from a rectangular waveguide into half-space through a rectangular aperture," tech. rep. tr-76-5 contract f 19628-73-c-0047, Airforce Cambridge Res. Lab, May 1976.

[10] R. F. Harrington and J. R. Mautz, "A generalized network formulation for the aperture problems," *IEEE Trans. Antennas Propagat.*, vol. AP-24, pp. 870–873, Nov. 1976.

[11] S. N. Sinha, D. K. Mehra, and R. P. Agarwal, "Radiation from a waveguide-backed aperture in an infinite ground plane in the presence of a thin conducting plate," *IEEE Trans. Antennas Propagat.*, vol. AP-34, pp. 539–545, Apr. 1986.

[12] J. A. Encinar and J. M. Rebollar, "A hybrid technique for analyzing corrugated and noncorrugated rectangular horns," *IEEE Trans. Antennas Propagat.*, vol. AP-34, pp. 961–968, Aug. 1986.

[13] T. Wriedt, K. H. Wolff, F. Arndt, and U. Tucholke, "Rigorous hybrid field theoretic design of stepped rectangular waveguide mode converters including the horn transitions into half-space," *IEEE Trans. Antennas Propagat.*, vol. AP-37, pp. 780–790, June 1989.

[14] H. Moheb and L. Shafai, "Applications of integral equations to numerical solution of radiation from horns.," *Program and Abstracts of North American Radio Science Meeting*, vol. London, Ontario, Canada, p. 285, June 1991.

[15] D. S. Katz, M. J. Piket-May, A. Taflove, and K. R. Umashankar, "FDTD analysis of electromagnetic wave radiation from systems containing horn antennas," *IEEE Trans. Antennas Propagat.*, vol. AP-39, pp. 1203–1212, Aug. 1991.

[16] P. A. Tirkas and C. A. Balanis, "Finite-difference time-domain method for antenna radiation," *IEEE Trans. Antennas Propagat.*, vol. AP-40, pp. 334–340, Mar. 1992.

[17] T. Wang, R. R. Harrington, and J. R. Mautz, "Electromagnetic scattering from and transmission through arbitrary apertures in conducting bodies," *IEEE Trans. Antennas Propagat.*, vol. AP-38, pp. 1805–1814, Nov. 1990.

[18] E. Kühn and V. Hombach, "Computer-aided analysis of corrugated horns with axial or ring-loaded radial slots," *Proc. ICAP 83 part 1*, pp. 127–131, 1983.

[19] H. Patzelt and F. Arndt, "Double-plane steps in rectangular waveguides and their application for transformers, irises, and filters," *IEEE Trans. Microwave Theory Tech.*, vol. MTT-30, pp. 771–776, May 1982.

[20] S. S. Saad, J. B. Davies, and O. J. Davies, "Computer analysis of gradually tapered waveguide with arbitrary cross-sections," *IEEE Trans. Microwave Theory Tech.*, vol. MTT-25, pp. 437–440, May 1977.

[21] F. Sporleder and H.-G. Unger, *Waveguide tapers transitions and couplers.* Peter Peregrinus Ltd., London, 1979.

[22] W. A. Huting and K. J. Webb, "Numerical solution of the continuous waveguide transition problem," *IEEE Trans. Microwave Theory Tech.*, vol. MTT-37, pp. 1802–1808, Nov. 1989.

[23] H. Flügel and E. Kühn, "Computer-aided analysis and design of circular waveguide tapers," *IEEE Trans. Microwave Theory Tech.*, vol. MTT-36, pp. 332–336, Feb. 1988.

[24] C. A. Balanis, *Advanced Engineering Electromagnetics.* Wiley, 1989.

[25] G. H. Golub and C. F. Van Loan, *Matrix Computations.* The Johns Hopkins University Press, 1989.

[26] F. X. Canning, "Direct solution of the EFIE with half the computation," *IEEE Trans. Antennas Propagat.*, vol. AP-39, pp. 118–119, Jan. 1991.

List of Tables

List of Figures

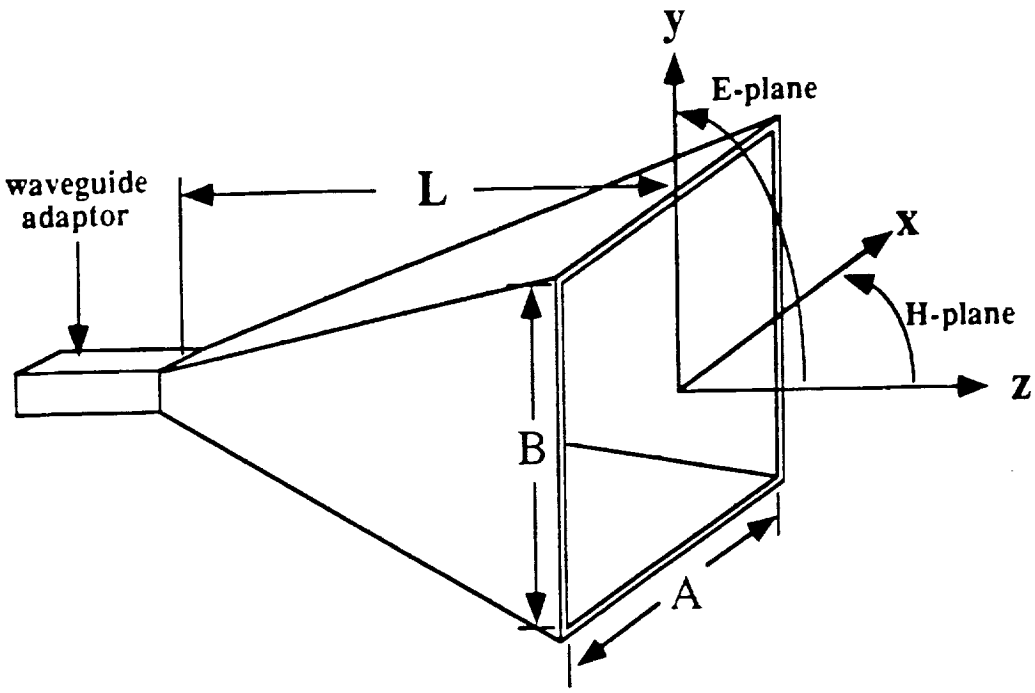

Figure 1. Geometry of the pyramidal horn antenna.

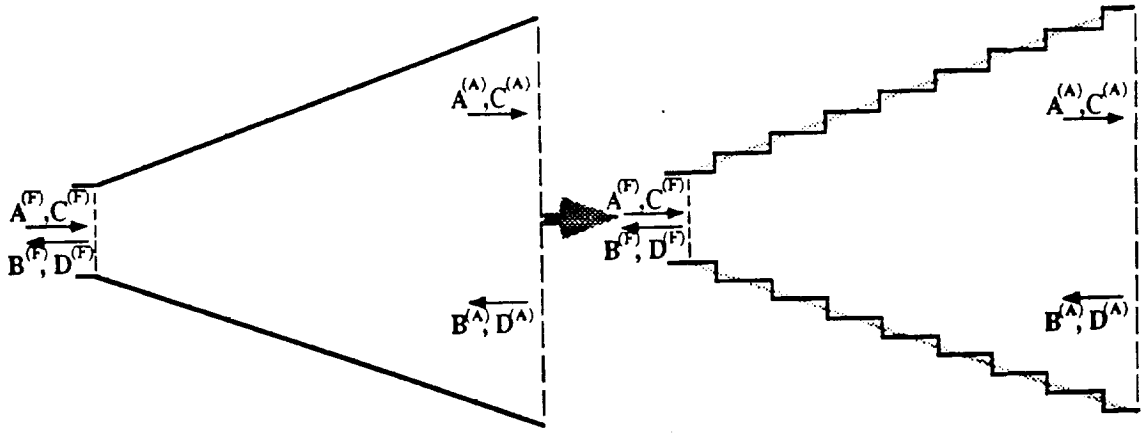

Figure 2. Stepped-waveguide model of the continuous horn transition.

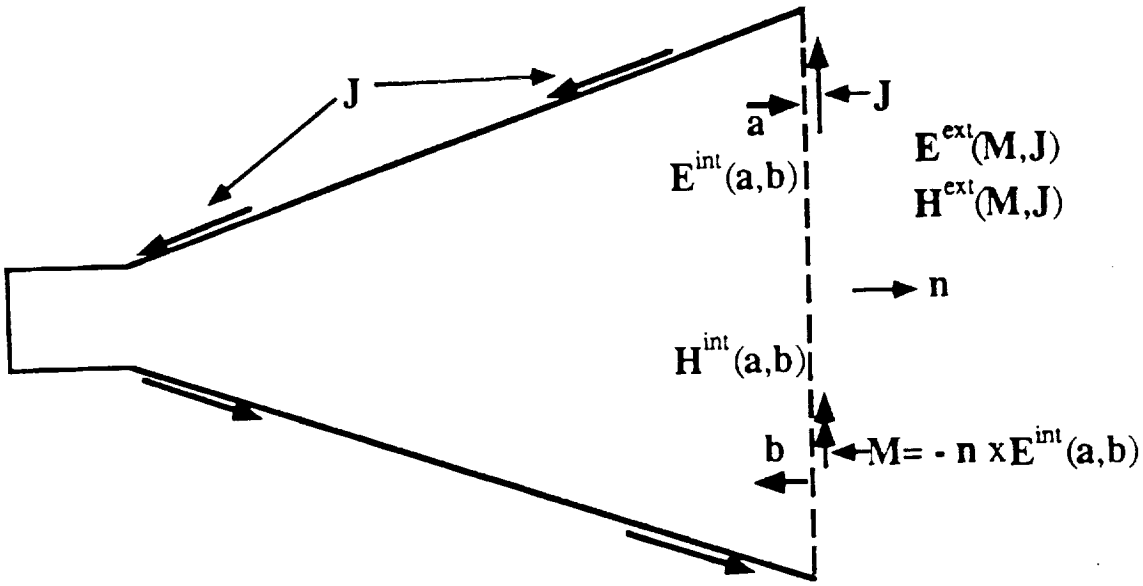

Figure 3. HFIE model of the outside surface of the pyramidal horn.

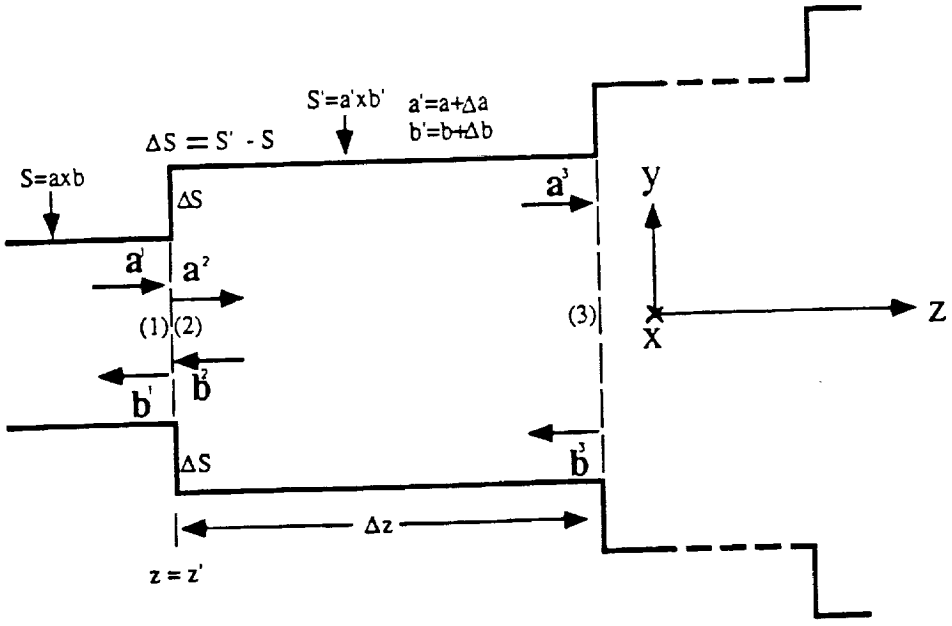

Figure 4. Field transition in a stepped waveguide junction.

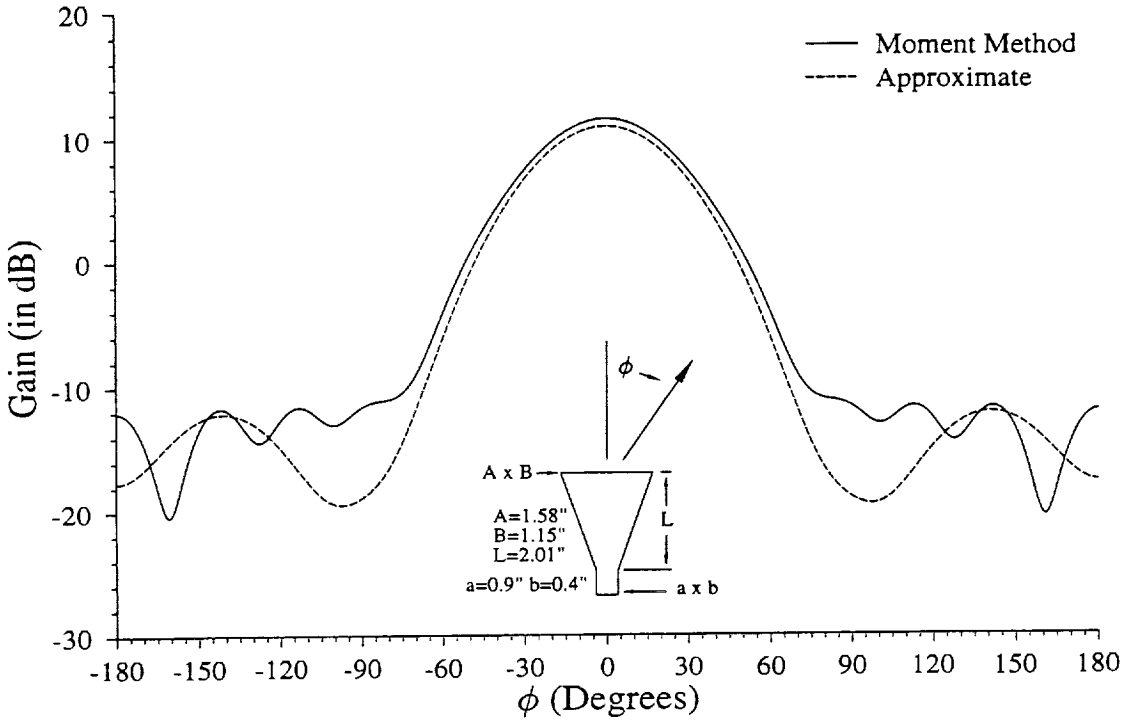

(a) E-plane

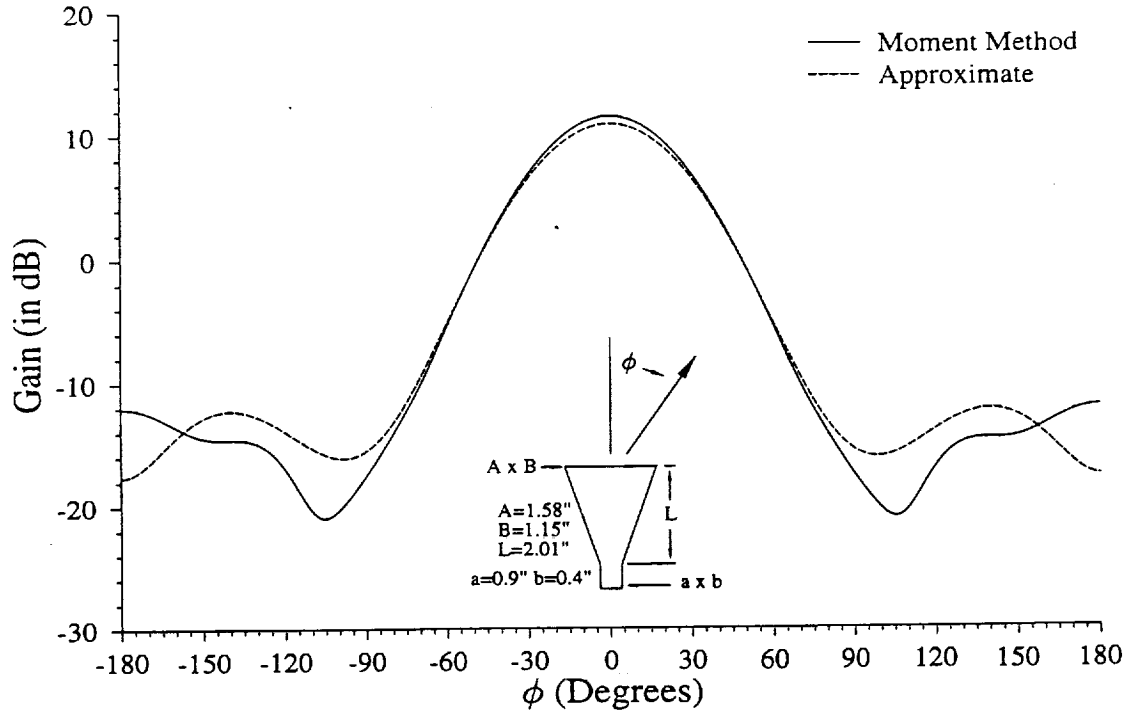

(b) H-plane

Figure 5. Comparison of E- and H-plane patterns for 10-dB standard gain horn at 10 GHz.

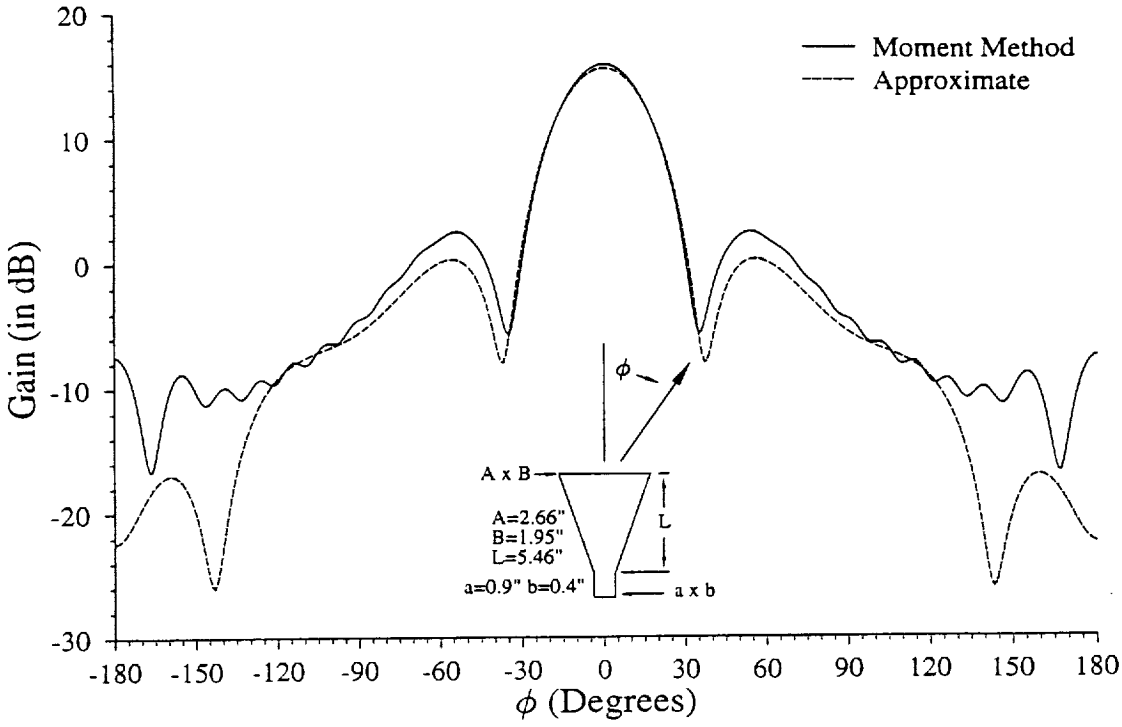

(a) E-plane

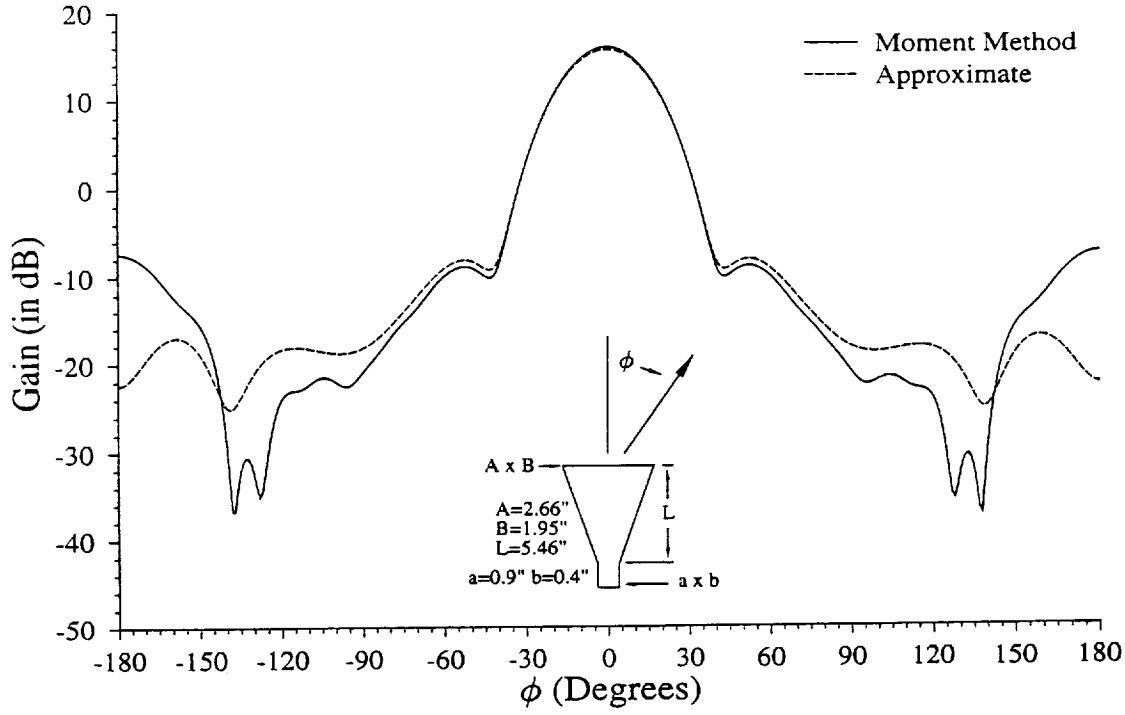

(b) H-plane

Figure 6. Comparison of E- and H-plane patterns for 15-dB standard gain horn at 10 GHz.

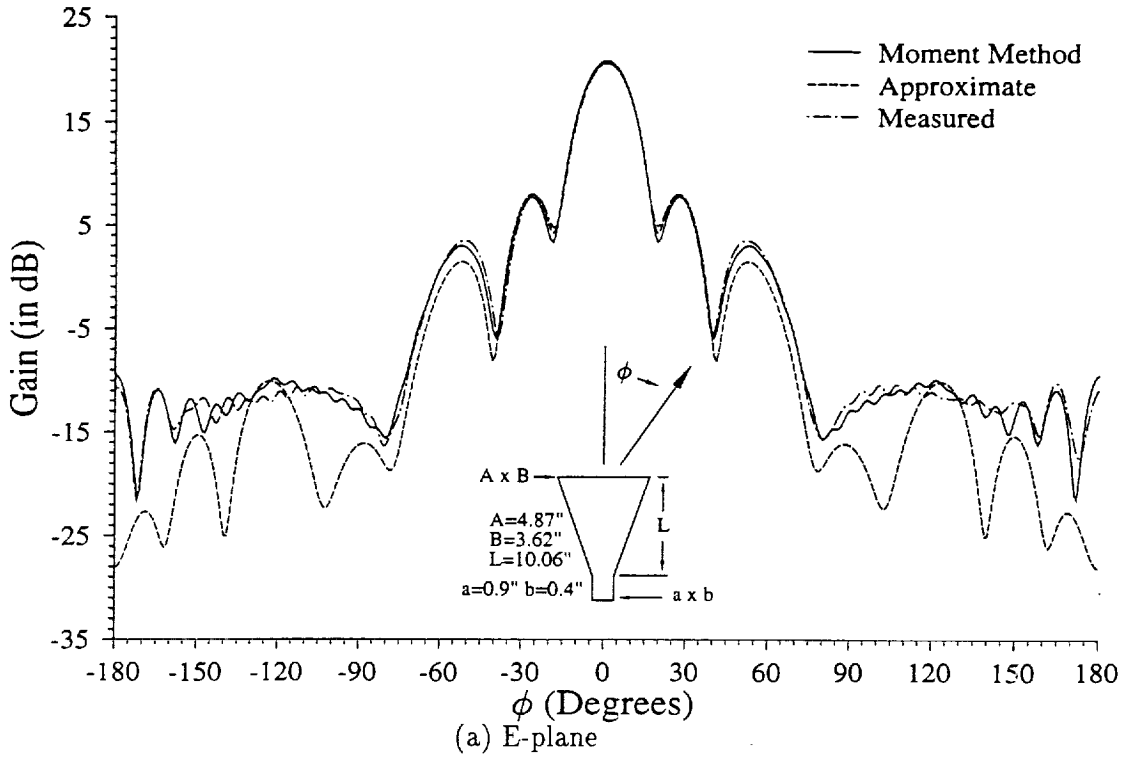

(a) E-plane

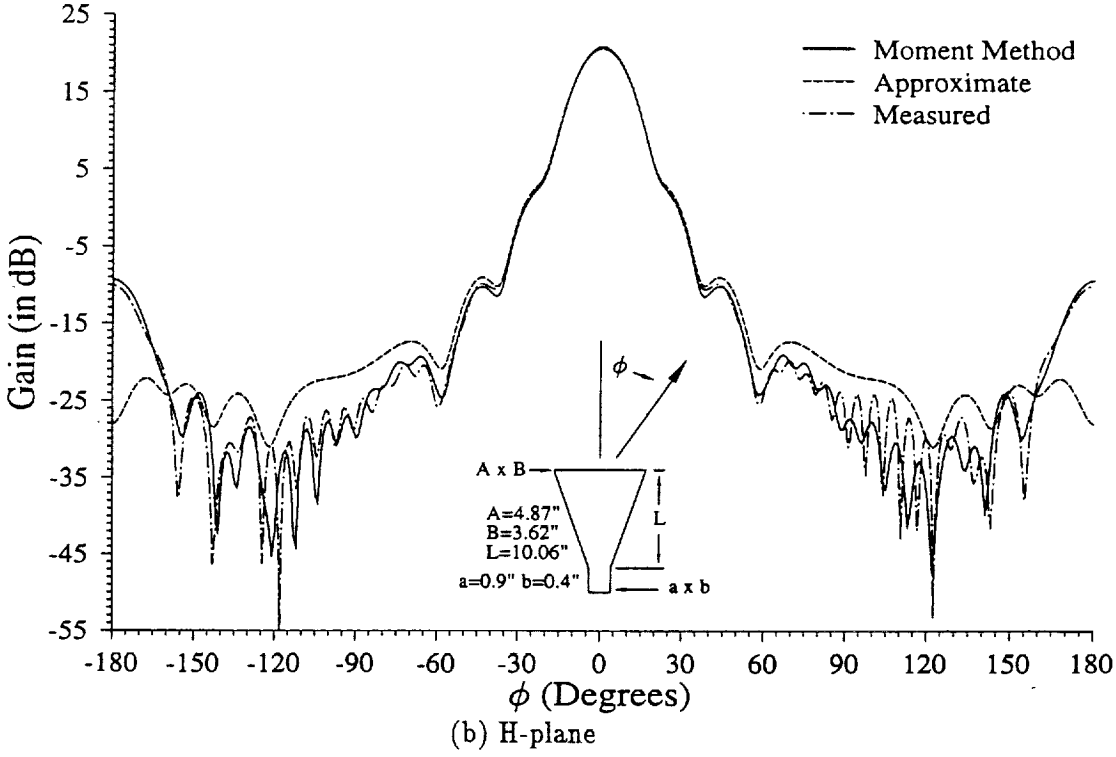

(b) H-plane

Figure 7. Comparison of E- and H-plane patterns for 20-dB standard-gain horn at 10 GHz.

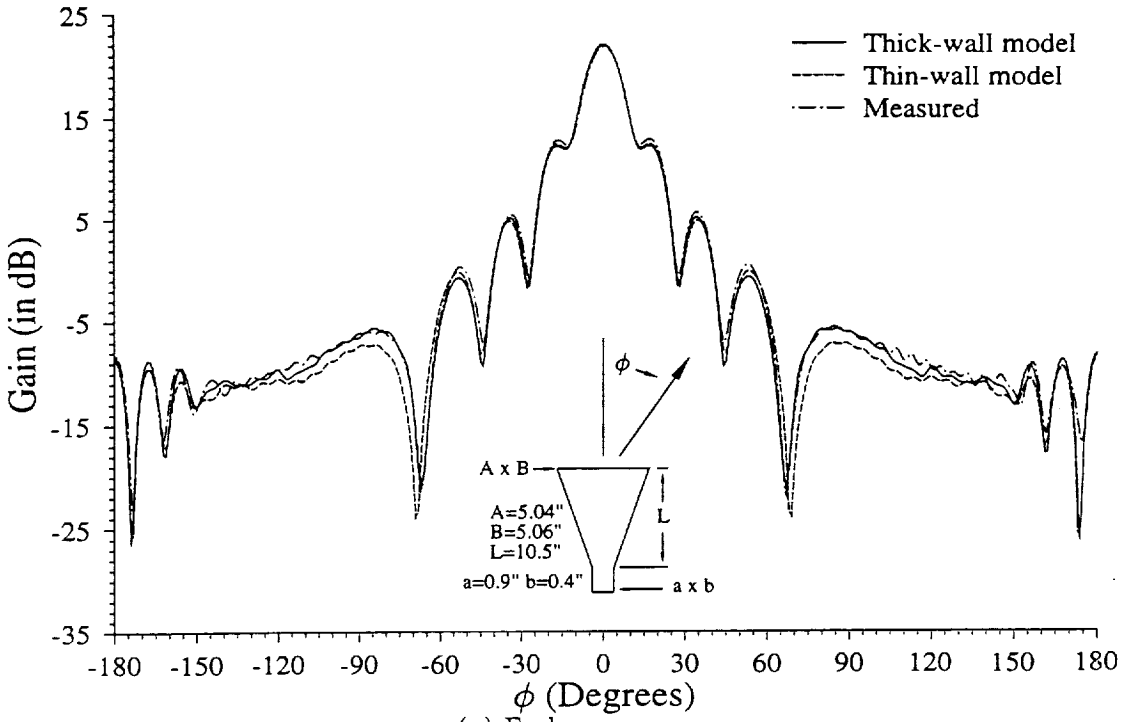

(a) E-plane

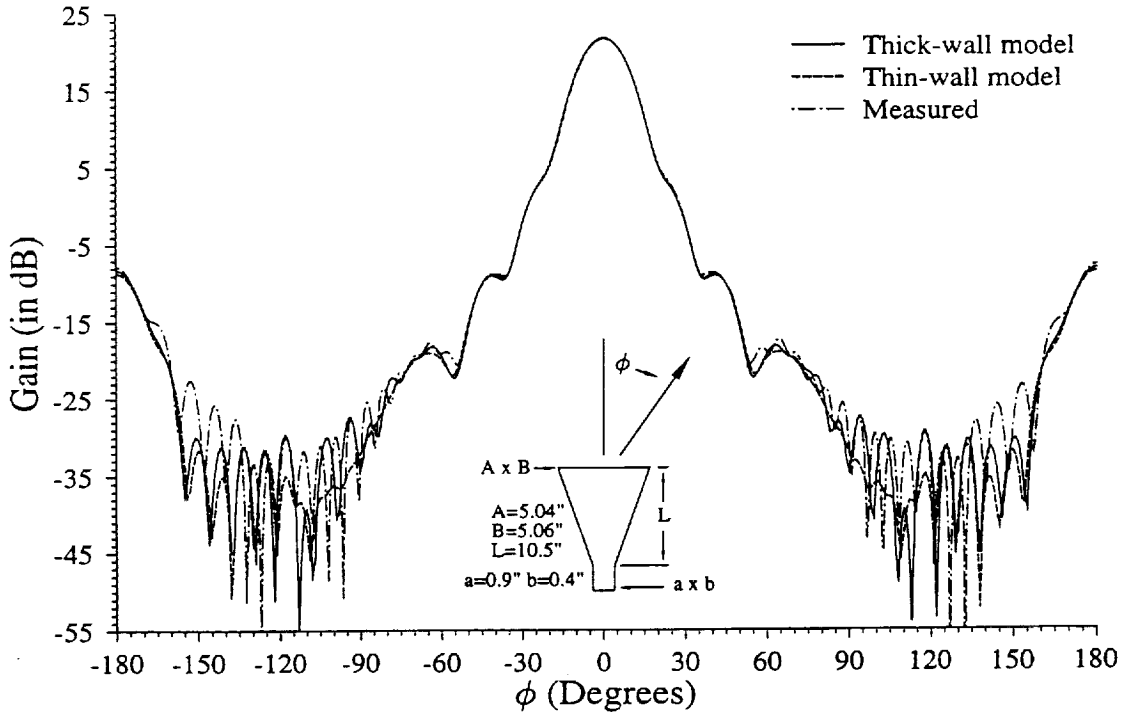

(b) H-plane

Figure 8. Comparison of E- and H-plane patterns for different aperture wall models of 5-inch horn at 10 GHz.

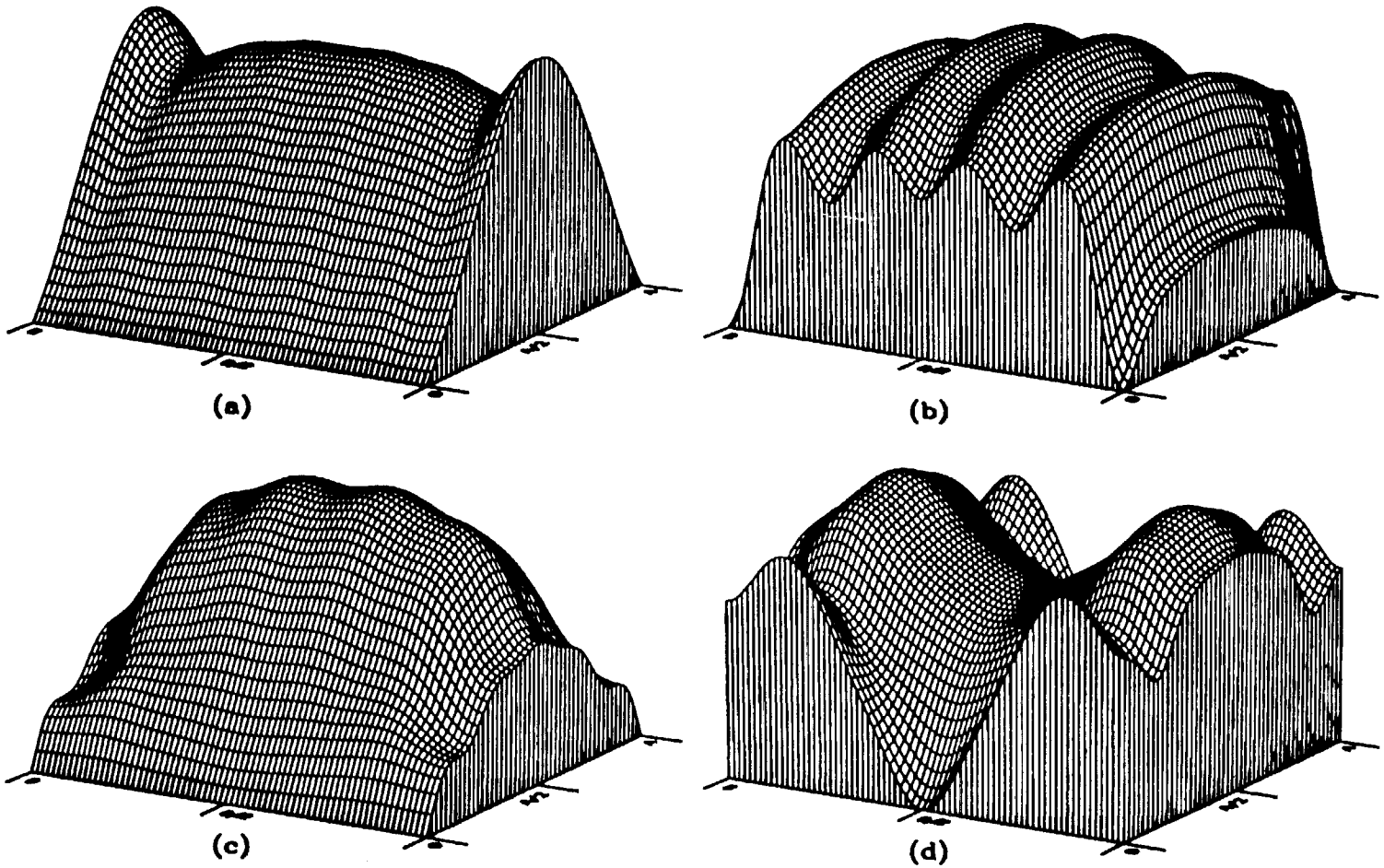

Figure 9. Aperture fields of 10-dB standard gain horn at 10 GHz.
(a), (b)--Magnitude and phase distributions of E_y
(c), (d)--Magnitude and phase distributions of H_x

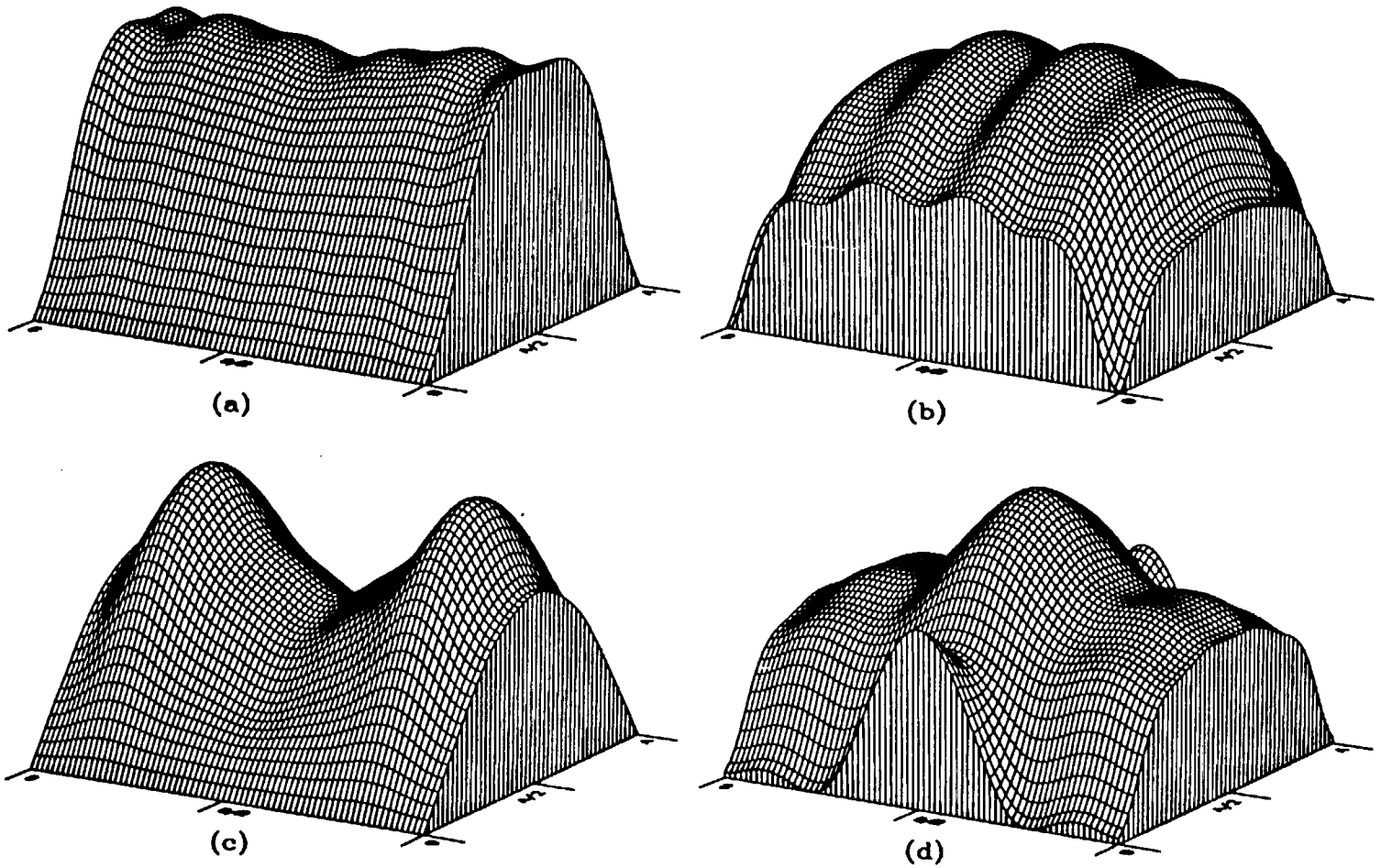

Figure 10. Aperture fields of 15-dB standard gain horn at 10 GHz.
(a), (b)--Magnitude and phase distributions of E_y
(c), (d)--Magnitude and phase distributions of H_x

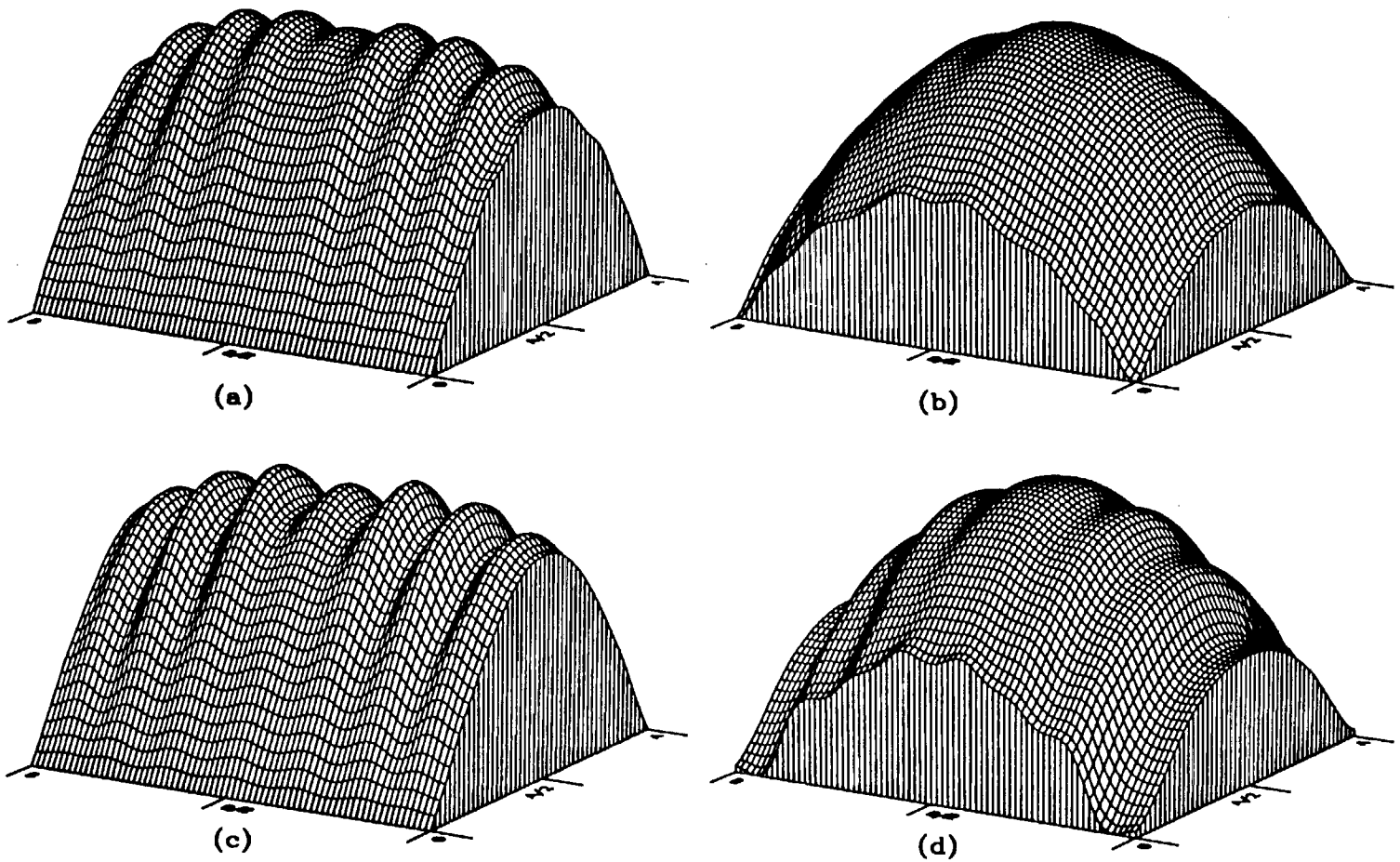

Figure 11. Aperture fields of 7-inch square horn at 10 GHz.
(a), (b)--Magnitude and phase distributions of E_y
(c), (d)--Magnitude and phase distributions of H_x